

# Linear Density Perturbations in Multifield Coupled Quintessence

Alexander Leithes,<sup>1</sup> Karim A. Malik,<sup>1</sup> David J. Mulryne,<sup>1</sup> and Nelson J. Nunes<sup>2</sup>

<sup>1</sup>*Astronomy Unit, School of Physics and Astronomy,  
Queen Mary University of London, Mile End Road, London, E1 4NS, UK*

<sup>2</sup>*Instituto de Astrofísica e Ciências do Espaço, Universidade de Lisboa,  
Faculdade de Ciências, Campo Grande, PT1749-016 Lisboa, Portugal*

(Dated: March 8, 2022)

We study the behaviour of linear perturbations in multifield coupled quintessence models. Using gauge invariant linear cosmological perturbation theory we provide the full set of governing equations for this class of models, and solve the system numerically. We apply the numerical code to generate growth functions for various examples, and compare these both to the standard  $\Lambda$ CDM model and to current and future observational bounds. Finally, we examine the applicability of the “small scale approximation”, often used to calculate growth functions in quintessence models, in light of upcoming experiments such as SKA and Euclid. We find the deviation of the full equation results for large  $k$  modes from the approximation exceeds the experimental uncertainty for these future surveys. The numerical code, PYESSENCE, written in Python will be publicly available.

## I. INTRODUCTION

The  $\Lambda$ CDM model of cosmology has become our gold standard in explaining the evolution of the universe. In this model, the dark sector of the universe is modelled by a cosmological constant, which is responsible for the acceleration of the universe in the present epoch, and a pressureless fluid that constitutes dark matter. The model is completed by assuming the presence of a baryonic matter and a radiation component. Remarkably, this simple picture is sufficient to explain most observational probes to date. These include high precision measurements of the CMB [1–3], supernovae observations [4–6], and large scale structure surveys [7–9].

Despite its success, the model raises many unanswered questions such as: Why does the cosmological constant take such an unnaturally small value? What is the fundamental nature of dark energy? These, in addition to other questions such as why the energy density associated with  $\Lambda$  is of the same order as that of dark matter - the coincidence problem - have lead the community to investigate more complex scenarios. One example is coupled quintessence. In this model a scalar field, which makes up the dark energy (DE) component of the universe and produces acceleration, is coupled to a pressureless dark matter fluid [10–23]. Recent extensions which have been investigated include Multi-coupled Dark Energy (McDE) (see e.g. Ref. [24]), in which the dark matter component of the universe is formed from two fluids that couple differently to a single scalar field.

In a series of recent papers [20, 21, 24], perturbations in the McDE model have been calculated numerically and compared with present and future large scale structure experiments. Taking this line of investigation, one can model the dark sector of the universe as being made up of  $N$  fluids interacting with  $M$  scalar fields. This model is known as Multifield or Assisted coupled quintessence [16]. The name derives from the idea that the many fields can act together to generate acceleration, in a similar manner to assisted inflation models of the early universe (see for example [25–27]).

Multifield coupled quintessence (M $\phi$ cQ) is the focus of the present paper. Our aims are two-fold. First we will calculate the equations of motion for linear perturbations in this rather general model, and incorporate these into a fast numerical code, PYESSENCE. In principal, this code can be used to generate quantities such as the growth factor of large scale structure for any coupled quintessence model with an arbitrary number of fields and fluids and arbitrary couplings. We intend to make this code publicly available. Secondly, we will apply this code, initially to revisit the McDE model, and then to consider specific models in which two scalar fields are present. Ongoing and future large scale surveys (see for example Refs. [28, 29]) offer a chance to distinguish between a cosmological constant and dynamical DE models, and it is important therefore to understand at what level the predictions of Multifield models will differ from those of  $\Lambda$ CDM and those of other quintessence models. In our work we adopt a phenomenological approach as is common in research conducted in this field. As such we have assumed that whatever the underlying particle theory may be, it includes mechanisms for screening quantum effects or other artefacts of the theory which might render it incompatible with observations. However see e.g. Refs. [30, 31] for possible difficulties in this approach.

For scales which are small compared to the horizon size today, an approximation to the full perturbed equations of motion has often been used in previous literature, and in particular in the previous study of McDE. A final aim of our work is to evaluate whether this approximation is sufficiently accurate, especially in the light of upcoming surveys.

The rest of this paper is set out as follows. Section II A contains the background equations. Section II B 1 contains the general gauge unspecified perturbed equations. Subsection II B 2 describes fixing the gauge in order that the equations can be solved numerically. Section III then describes the resulting PYESSENCE code. Section IV reviews

the observational quantities against which our results can be compared. Finally, section V details our numerical investigation of specific M $\varphi$ cQ and related models. We conclude in Section VII.

## II. THE MODEL

In this paper, the dark sector of the universe is modelled by  $N$  different dark matter fluids, with arbitrary equation of state, and  $M$  different scalar fields. We also include two further fluids which model baryonic matter, and radiation. The general energy-momentum tensor for any perfect fluid is given by

$$T_{\nu}^{\mu(M_{\alpha})} = (\rho_{\alpha} + P_{\alpha})u_{(\alpha)}^{\mu}u_{\nu(\alpha)} + \delta_{\nu}^{\mu}P_{\alpha}, \quad (2.1)$$

where the subscript  $\alpha$  labels the  $N + 2$  fluids,  $\rho_{\alpha}$  is the density of any given fluid and  $P_{\alpha}$  the corresponding pressure, and  $u_{(\alpha)}^{\mu}$  is the four velocity for a given fluid. The equation of state is defined as,

$$w_{\alpha} = \frac{P_{\alpha}}{\rho_{\alpha}}. \quad (2.2)$$

Here and throughout Greek indices  $\mu$  and  $\nu$  label coordinates running over time and relative dimensions in space, and we use lower case Latin indices to label only spatial dimensions. The energy-momentum tensor for the scalar fields is given by

$$T_{\nu}^{\mu(\varphi)} = g^{\lambda\mu} \sum_I \partial_{\lambda}\varphi_I \partial_{\nu}\varphi_I - \delta_{\nu}^{\mu} \left( \frac{1}{2} \sum_I g^{\rho\sigma} \partial_{\rho}\varphi_I \partial_{\sigma}\varphi_I + V(\phi_1, \dots, \phi_M) \right), \quad (2.3)$$

where  $V$  is the potential energy, and upper case Roman indices label the  $M$  fields. In order to model the interaction of the matter fluids with the scalar fields, we assume [10, 16]

$$\nabla_{\mu}T_{\nu}^{\mu(\varphi)} = \kappa \sum_{\alpha, I} \mathbb{C}_{I\alpha} T_{(M_{\alpha})} \nabla_{\nu}\varphi_I \quad , \quad \nabla_{\mu}T_{\nu}^{\mu(M_{\alpha})} = -\kappa \sum_I \mathbb{C}_{I\alpha} T_{(M_{\alpha})} \nabla_{\nu}\varphi_I, \quad (2.4)$$

where  $\kappa = (8\pi G)^{\frac{1}{2}}$  and  $\mathbb{C}_{I\alpha}$  are coupling constants. Here  $T_{(M_{\alpha})}$  is the trace of Energy-momentum tensor,

$$T_{(M_{\alpha})} = T_{\mu(M_{\alpha})}^{\mu}, \quad (2.5)$$

for a given fluid. Equations Eq. (2.4) respect energy-momentum conservation of the total matter content. In what follows we will set the relevant components of the  $C$  matrix such that there is no interaction between baryons or radiation and the scalar fields.

### A. Background cosmology

We take a flat Friedmann-Lemaître-Robertson-Walker (FLRW) spacetime as our background with line element

$$ds^2 = -dt^2 + a^2(t)\delta_{ij}dx^i dx^j, \quad (2.6)$$

where  $a(t)$  is the scale factor,  $t$  is cosmic time, and assume the fluids to be comoving with the expansion of the universe such that

$$\bar{u}_{0(\alpha)} = -1 \quad , \quad \bar{u}_{i(\alpha)} = 0. \quad (2.7)$$

Here we use “bars” to denote background quantities. The background stress energy tensor for the fluids then becomes

$$\bar{T}_{00} = \sum_{\alpha} \bar{\rho}_{\alpha} + \sum_I \frac{\dot{\bar{\varphi}}_I^2}{2} + V \quad , \quad \bar{T}_{0j} = 0 \quad , \quad \bar{T}_{ij} = \delta_{ij}a^2 \left( \sum_{\alpha} \bar{P}_{\alpha} + \sum_I \frac{\dot{\bar{\varphi}}_I^2}{2} - V \right), \quad (2.8)$$

where an overdot indicates a derivative with respect to cosmic time. Eq. (2.4) leads to the evolution equation for each fluid

$$\dot{\bar{\rho}}_{\alpha} + 3H(\bar{\rho}_{\alpha} + \bar{P}_{\alpha}) = -\kappa \sum_I \mathbb{C}_{I\alpha} (\bar{\rho}_{\alpha} - 3\bar{P}_{\alpha}) \dot{\bar{\varphi}}_I, \quad (2.9)$$

where  $H$  is the Hubble parameter, and to the Klein-Gordon equation for each field

$$\ddot{\bar{\varphi}}_I + 3H\dot{\bar{\varphi}}_I + V_{,\varphi_I} = \kappa \sum_{\alpha} \mathbb{C}_{I\alpha}(\bar{\rho}_{\alpha} - 3\bar{P}_{\alpha}). \quad (2.10)$$

The background Friedmann equation is

$$H^2 = \frac{\kappa^2}{3} \left[ \sum_{\alpha} \bar{\rho}_{\alpha} + \sum_I \frac{\dot{\bar{\varphi}}_I^2}{2} + V \right]. \quad (2.11)$$

Finally, we define the density parameter

$$\Omega_{\alpha} = \frac{\bar{\rho}_{\alpha}}{\rho_c}, \quad (2.12)$$

where  $\rho_c$  is the critical density defined as

$$\rho_c = \frac{3H^2}{\kappa^2}. \quad (2.13)$$

## B. Linear perturbations

### 1. General Perturbed Equations Gauge Unspecified

The line element for perturbations about a flat FLRW spacetime with the gauge unspecified is given by [32]

$$ds^2 = -(1+2\phi)dt^2 + 2aB_{,i}dtdx^i + a^2(1+2C_{ij})dx^i dx^j, \quad (2.14)$$

where  $\phi$  is the lapse function,  $B$  the shift function and partial derivatives are denoted by a ‘‘comma’’. We can make the further decomposition to  $C_{ij} = E_{,ij} - \psi\delta_{ij}$ , where we have kept only scalar parts. The perturbed 4-velocity [32] is

$$u_0 = -(1+\phi), \quad u_i = a(v+B)_{,i}, \quad (2.15)$$

and the total perturbed energy-momentum tensor for our model is given by

$$\begin{aligned} \delta T_{00} &= \sum_{\alpha} \delta\rho_{\alpha} + \sum_I (-\phi\dot{\bar{\varphi}}_I^2 + \delta\varphi_I\dot{\bar{\varphi}}_I + V_{,\varphi_I}\delta\varphi_I), \\ \delta T_{0j} &= a \left[ \sum_I \dot{\bar{\varphi}}_I \left( \dot{\bar{\varphi}}_I B_{,i} + \frac{1}{a}\delta\varphi_{I,i} \right) - \sum_{\alpha} (\bar{\rho}_{\alpha} + \bar{P}_{\alpha})v_{(\alpha),i} \right], \\ \delta T_{ij} &= \delta_{ij}a^2 \left( \sum_{\alpha} \delta P_{\alpha} - \sum_I (\phi\dot{\bar{\varphi}}_I^2 - \delta\varphi_I\dot{\bar{\varphi}}_I + V_{,\varphi_I}\delta\varphi_I) \right). \end{aligned} \quad (2.16)$$

Moving to Fourier space, the evolution equations for density fluctuations are given by

$$\dot{\delta\rho}_{\alpha} - \left( \frac{k^2 v_{\alpha}}{a} + k^2 \dot{E} + 3\dot{\psi} \right) (\bar{\rho}_{\alpha} + \bar{P}_{\alpha}) + 3H(\delta\rho_{\alpha} + \delta P_{\alpha}) = -\kappa \sum_I \mathbb{C}_{I\alpha}(\bar{\rho}_{\alpha} - 3\bar{P}_{\alpha})\dot{\delta\varphi}_I - \kappa \sum_I \mathbb{C}_{I\alpha}(\delta\rho_{\alpha} - 3\delta P_{\alpha})\dot{\bar{\varphi}}_I, \quad (2.17)$$

momentum conservation gives the constraint

$$\dot{v}_{\alpha} = \kappa \sum_I \mathbb{C}_{I\alpha}(\bar{\rho}_{\alpha} - 3\bar{P}_{\alpha})\frac{\delta\varphi_I}{a} + 3H\frac{\dot{\bar{P}}_{\alpha}}{\bar{\rho}_{\alpha}}(v_{\alpha} + B) - H(v_{\alpha} + B) - \frac{\dot{\phi}}{a} - \frac{\delta P_{\alpha}}{a(\bar{\rho}_{\alpha} + \bar{P}_{\alpha})} - \dot{B}, \quad (2.18)$$

and the evolution of scalar field perturbations is given by

$$\begin{aligned} \ddot{\delta\varphi}_I + 3H\dot{\delta\varphi}_I + \sum_J V_{,\varphi_I\varphi_J}\delta\varphi_J - (k^2\dot{E} + 3\dot{\psi})\dot{\bar{\varphi}}_I + \frac{k^2}{a^2}\delta\varphi_I + \frac{\dot{\bar{\varphi}}_I}{a}k^2B - \dot{\bar{\varphi}}_I\dot{\phi} + 2V_{,\varphi_I}\phi \\ - 2\kappa \sum_{\alpha} \mathbb{C}_{I\alpha}(\bar{\rho}_{\alpha} - 3\bar{P}_{\alpha})\phi - \kappa \sum_{\alpha} \mathbb{C}_{I\alpha}(\delta\rho_{\alpha} - 3\delta P_{\alpha}) = 0. \end{aligned} \quad (2.19)$$

The Einstein Field Equations are as follows. From the  $0 - 0$  component we get

$$3H(\dot{\psi} + H\phi) + \frac{k^2}{a^2}(\psi + H[a^2\dot{E} - aB]) = -\frac{\kappa^2}{2} \left[ \sum_{\alpha} \delta\rho_{\alpha} + \sum_I (-\phi\dot{\bar{\varphi}}_I^2 + \dot{\delta\varphi}_I\dot{\bar{\varphi}}_I + V_{,\varphi_I} \delta\varphi_I) \right], \quad (2.20)$$

from the  $0 - i$  component

$$\dot{\psi} + H\phi = -\frac{\kappa^2}{2} \left[ \sum_{\alpha} a(v_{\alpha} + B)(\bar{\rho}_{\alpha} + \bar{P}_{\alpha}) - \sum_I \dot{\bar{\varphi}}_I \delta\varphi_I \right], \quad (2.21)$$

from the trace of the  $i - j$  component

$$\ddot{\psi} + 3H\dot{\psi} + H\dot{\phi} + (3H^2 + 2\dot{H})\phi = \frac{\kappa^2}{2} \left[ \sum_{\alpha} \delta P_{\alpha} + \sum_I (-\phi\dot{\bar{\varphi}}_I^2 + \dot{\delta\varphi}_I\dot{\bar{\varphi}}_I - V_{,\varphi_I} \delta\varphi_I) \right], \quad (2.22)$$

and from the trace-free part of the  $i - j$  component

$$\dot{\sigma}_s + H\sigma_s - \phi + \psi = 0, \quad (2.23)$$

where  $\sigma_s$  is the scalar shear and  $\sigma_s = a^2\dot{E} - aB$ .

## 2. Governing equations in flat gauge

Many gauge choices are available. Previously in the literature a common choice of gauge for studies of coupled quintessence models has been the longitudinal gauge ( $\tilde{B} = \tilde{E} = 0$ ), and we present the equations of motion for perturbations in this gauge in Appendix B. However, we found that this gauge is not a good choice for the numerical integration of the full equations of motion. This is due to the prefactor term in Eq. (B8). The magnitude of the second term in this prefactor is orders of magnitude smaller than the first, except when the first touches zero, which can occur as the fields oscillate. This leads to a loss of accuracy at these times and to a numerical instability. For our numerical integration we therefore use the flat gauge which does not suffer from this problem.

The flat gauge is defined by the conditions  $\psi = 0$  and  $\tilde{E} = 0$ . Defining the new quantity

$$\hat{v}_{\alpha} = v_{\alpha} + B, \quad (2.24)$$

in this gauge, Eq. (2.17) reduces to

$$\delta\dot{\rho}_{\alpha} + 3H(\delta\rho_{\alpha} + \delta P_{\alpha}) - \frac{k^2(\hat{v}_{\alpha} - B)}{a}(\bar{\rho}_{\alpha} + \bar{P}_{\alpha}) = -\sum_I \kappa \mathbb{C}_{I\alpha}(\bar{\rho}_{\alpha} - 3\bar{P}_{\alpha})\dot{\delta\varphi}_I - \sum_I \kappa \mathbb{C}_{I\alpha}(\delta\rho_{\alpha} - 3\delta P_{\alpha})\dot{\bar{\varphi}}_I, \quad (2.25)$$

and Eq. (2.18) to

$$\dot{\hat{v}}_{\alpha} = \kappa \sum_I \mathbb{C}_{I\alpha}(\bar{\rho}_{\alpha} - 3\bar{P}_{\alpha})\frac{\delta\varphi_I}{a} + 3H\frac{\dot{\bar{P}}_{\alpha}}{\dot{\bar{\rho}}_{\alpha}}\hat{v}_{\alpha} - H\hat{v}_{\alpha} - \frac{\phi}{a} - \frac{\delta P_{\alpha}}{a(\bar{\rho}_{\alpha} + \bar{P}_{\alpha})}. \quad (2.26)$$

The evolution equation for the fields, Eq. (2.19), becomes

$$\begin{aligned} & \delta\ddot{\varphi}_I + 3H\delta\dot{\varphi}_I + \sum_J V_{,\varphi_I\varphi_J} \delta\varphi_J - \left[ \frac{\kappa^2}{2H} \left( \sum_{\alpha} \delta P_{\alpha} - \sum_I (\phi\dot{\bar{\varphi}}_I^2 - \dot{\delta\varphi}_I\dot{\bar{\varphi}}_I + V_{,\varphi_I} \delta\varphi_I) \right) - \frac{(3H^2 + 2\dot{H})}{H} \phi \right] \dot{\bar{\varphi}}_I \\ & + \frac{k^2}{a^2} \delta\varphi_I + \frac{k^2 B}{a} \dot{\bar{\varphi}}_I + 2V_{,\varphi_I} \phi - 2 \sum_{\alpha} \kappa \mathbb{C}_{I\alpha}(\bar{\rho}_{\alpha} - 3\bar{P}_{\alpha})\phi - \sum_{\alpha} \kappa \mathbb{C}_{I\alpha}(\delta\rho_{\alpha} - 3\delta P_{\alpha}) = 0. \end{aligned} \quad (2.27)$$

From Eq. (2.20), we get

$$3H^2\phi - \frac{k^2 B}{a} H = -\frac{\kappa^2}{2} \left[ \sum_{\alpha} \delta\rho_{\alpha} + \sum_I (-\phi\dot{\bar{\varphi}}_I^2 + \dot{\delta\varphi}_I\dot{\bar{\varphi}}_I + V_{,\varphi_I} \delta\varphi_I) \right], \quad (2.28)$$

and from Eq. (2.21)

$$\phi = -\frac{\kappa^2}{2H} \left[ \sum_{\alpha} a \hat{v}_{\alpha} (\bar{\rho}_{\alpha} + \bar{P}_{\alpha}) - \sum_I \dot{\bar{\varphi}}_I \delta\varphi_I \right], \quad (2.29)$$

which allows us to replace  $\phi$  in terms of field and fluid perturbations. For completeness we note that Eq. (2.22) gives

$$H\dot{\phi} + (3H^2 + 2\dot{H})\phi = \frac{\kappa^2}{2} \left[ \sum_{\alpha} \delta P_{\alpha} - \sum_I \left( \phi \dot{\bar{\varphi}}_I^2 - \delta\dot{\varphi}_I \dot{\bar{\varphi}}_I + V_{,\varphi_I} \delta\varphi_I \right) \right] \quad (2.30)$$

and from Eq. (2.23) we have

$$\dot{B} + 2HB = -\frac{\phi}{a}. \quad (2.31)$$

Combining Eq. (2.28) and Eq. (2.29) we find

$$B = \frac{3\kappa^2 a}{2k^2} \left[ \frac{1}{3H} \left( \sum_{\alpha} \delta\rho_{\alpha} - \sum_I (\phi \dot{\bar{\varphi}}_I^2 - \delta\dot{\varphi}_I \dot{\bar{\varphi}}_I - V_{,\varphi_I} \delta\varphi_I) \right) + \sum_I \dot{\bar{\varphi}}_I \delta\varphi_I - \sum_{\alpha} a \hat{v}_{\alpha} (\bar{\rho}_{\alpha} + \bar{P}_{\alpha}) \right], \quad (2.32)$$

which allows us to replace  $B$  in terms of field and fluid perturbations.

### III. NUMERICAL SOLUTIONS

We can now solve the closed system of equations derived in the previous section numerically. The system of background equations for the scalar fields and the energy densities of the fluids, Eq. (2.9) and Eq. (2.10), together with the Friedmann constraint Eq. (2.11), is solved simultaneously with the evolution equations for the perturbations  $\delta\rho_{\alpha}$ ,  $\hat{v}_{\alpha}$  and  $\delta\varphi_I$ , Eq. (2.25) to Eq. (2.27), together with the constraint equations for  $\phi$  and  $B$ , Eq. (2.29) and Eq. (2.32). The numerical code, named PYESSENCE, is written in Python and publicly available on Bitbucket [33] and on the PYESSENCE website [34] under an open source modified BSD license, with documentation available in Ref. [35].

#### A. Initial Conditions

##### 1. Background Initial Conditions

We set the initial conditions for the background energy densities of the fluids and the background field amplitudes such that the background evolution follows closely that of the  $\Lambda$ CDM model. Due to the potentials used in the models tested we have analytical solutions for the background evolution equations, which enables us to set the background initial conditions in terms of their values today. We are free to choose an initial time, and select  $N = -14$ , which fixes the initial value for the scale factor  $a$  and coordinate time,  $t$ . This also ensures we are well into the radiation dominated epoch. In particular, we demand that the model satisfies constraints on present day energy densities from Planck data [36]. These are  $\Omega_{\Lambda} = 0.6911 \pm 0.0062$  for the cosmological constant,  $\Omega_r = 9.117 \times 10^{-5}$  for radiation,  $\Omega_b = 0.0486 \pm 0.0003$  for baryons and  $\Omega_{CDM} = 1 - \Omega_{DE} - \Omega_r - \Omega_b$  for cold dark matter. To do so, we assume that the scalar fields will collectively replace  $\Lambda$ , and the dark matter fluids collectively replace the single cold dark matter species of the  $\Lambda$ CDM model. Initially we take the fields' velocity to be zero,  $\dot{\varphi}_I = 0$ . Of course we need to check on a case by case basis whether the fields really do generate acceleration in a way that accounts for observations, and that dark matter components behave in a viable way, such that the background evolution is compatible with current limits.

##### 2. Perturbed Initial Conditions

We start our simulations at sufficiently early times to ensure radiation domination and that all the  $k$  modes studied lie outside the horizon at that time. For simplicity, we choose the initial conditions for the field velocity and field perturbations to be zero

$$\dot{\delta\varphi}_I = \delta\varphi_I = 0, \quad (3.1)$$

though we find the evolution is insensitive to this choice. The initial conditions for all other perturbations can be given in terms of observational constraints on the power spectrum of the gauge invariant curvature perturbation  $\zeta$ , (see for example Ref. [37]),

$$\langle \zeta^2 \rangle = \delta^3(\mathbf{k} - \mathbf{k}') \frac{2\pi^2}{k^3} \mathcal{P}_\zeta(k), \quad (3.2)$$

where  $\zeta$ , the curvature perturbation on uniform density hypersurfaces, is defined as

$$-\zeta = \psi + \frac{H}{\dot{\rho}} \delta\rho. \quad (3.3)$$

On superhorizon scales the power spectrum can be parametrised as

$$\mathcal{P}_\zeta(k) = A_s \left( \frac{k}{k_*} \right)^{n_s - 1}, \quad (3.4)$$

where [38]  $A_s = 2.142 \times 10^{-9}$  is the scalar amplitude at the Planck pivot scale  $k_* = 0.05 \text{ Mpc}^{-1}$ , and  $n_s = 0.9667$  is the spectral index [36].

From Eq. (3.3) we then get a relation between the curvature perturbation and the total energy density perturbation in flat gauge, such that,

$$\delta\rho_{\text{flat}} = -\frac{\dot{\rho}}{H} \zeta. \quad (3.5)$$

This allows us to set the initial condition for the individual fluids. In addition we assume that the initial conditions are adiabatic, which gives a relation between the fluid density perturbations initially. The gauge-invariant relative entropy perturbation between two non-interacting fluids [32] is given by

$$\mathcal{S}_{\alpha\beta} = -3H \left( \frac{\delta\rho_\alpha}{\dot{\rho}_\alpha} - \frac{\delta\rho_\beta}{\dot{\rho}_\beta} \right). \quad (3.6)$$

Adiabatic initial conditions require that  $\mathcal{S}_{\alpha\beta} = 0$ . Combining Eq. (3.6) with Eq. (2.9) for radiation and baryons, which for these models, as specified in Section I have couplings of zero, we find

$$\delta_b = \frac{3}{4} \delta_r, \quad (3.7)$$

where we introduced the density contrast for a given fluid species,  $\alpha$ , as

$$\delta_\alpha \equiv \frac{\delta\rho_\alpha}{\bar{\rho}_\alpha}. \quad (3.8)$$

Finally we can set the initial conditions for the 3-velocities,  $\hat{v}_\alpha$ . We checked numerically that the late time evolution of the system is not very sensitive to the actual value for the 3-velocities, and we therefore set  $\hat{v}_\alpha = 0$  initially. While studying the initial conditions we found that aside from the initial radiation density perturbation the results are fairly insensitive to small changes in the initial conditions, due to the integration starting well inside radiation domination. Small variations in the initial conditions for the other constituents, for a given  $k$  mode, soon converged to a common trajectory within approximately one e-fold from the start of the simulations. This meant there was negligible difference in the observable growth of the density perturbations.

### 3. Relating Longitudinal Gauge to Flat Gauge

In the previous sections we have presented the system of governing equations and the initial conditions for the code in flat gauge. However, in order to connect to previous studies in the literature we present our results in terms of the density contrast in longitudinal gauge.

Using the background and perturbed densities as defined in Eq. (2.8) and Eq. (2.16), the total density contrast is defined as,

$$\delta = \frac{\sum_\alpha \delta\rho_\alpha + \sum_I \delta\rho_{\varphi_I}}{\sum_\alpha \bar{\rho}_\alpha + \sum_I \bar{\rho}_{\varphi_I}}. \quad (3.9)$$

Using the transformations for the metric and matter variables given in appendix A 2, and the constraint Eqns. (2.32), we find

$$\delta_{\text{long}} = \delta_{\text{flat}} + \frac{\dot{\bar{\rho}}^2}{\bar{\rho}} a \left( \frac{3\kappa^2 a}{2k^2} \left[ \frac{1}{3H} \left( \sum_{\alpha} \delta\rho_{\alpha} - \sum_I (\phi\dot{\bar{\varphi}}_I^2 - \delta\varphi_I\dot{\bar{\varphi}}_I - V_{,\varphi_I} \delta\varphi_I) \right) + \sum_I \dot{\bar{\varphi}}_I \delta\varphi_I - \sum_{\alpha} a\hat{v}_{\alpha}(\bar{\rho}_{\alpha} + \bar{P}_{\alpha}) \right] \right), \quad (3.10)$$

which reduces initially to

$$\delta_{\text{long}} = \delta_{\text{flat}} + \left( \frac{k}{a} \right)^{-2} \left[ 4\pi G\delta_{\text{flat}} - \frac{\dot{\bar{\rho}}^2}{3H\bar{\rho}} a \sum_{\alpha} (\bar{\rho}_{\alpha} + \bar{P}_{\alpha}) \hat{v}_{\alpha} \right]. \quad (3.11)$$

#### IV. OBSERVATIONS

Two key parameters which are constrained by observational data are the growth factor and growth function. We therefore apply our code to calculate these quantities. The growth factor is defined as

$$g = \frac{\delta}{\delta_0}, \quad (4.1)$$

where  $\delta$  is the total density contrast defined in the longitudinal gauge [29], and  $\delta_0$  is the total density contrast today. The growth function,  $f$ , is defined as

$$f = \frac{\delta'}{\delta}, \quad (4.2)$$

where the prime in this case denotes a derivative with respect to the number of e-folds [29]. Typically observational results are presented as constraints on the combinations  $fg$  and  $f\sigma_8$ , since, for example, these quantities can be extracted directly from redshift space distortions (see e.g. [39]).  $\sigma_8$  is the amplitude of the matter power spectrum at a scale of  $8h^{-1}\text{Mpc}$  [29, 40]. The experimental uncertainty of  $\sigma_8$ , taken from DES, which overlaps two other data sets which are in some tension (CFHTLenS and Planck), is  $0.81^{+0.16}_{-0.26}$  [41]. In Subsection VB 4 we use  $\sigma_8 = 0.81$  [36] since this is consistent with the other Planck based parameter values we have used. Future surveys hope to have the sensitivity to pick up  $k$  dependence in the growth of structure. SKA [29, 39], for example, should be sensitive to measurements of growth at approximately the percent level (or better) for  $42H_0 < k < 420H_0$  at a redshift  $z \approx 1$  [39]. For  $k > 42H_0$  this sensitivity falls to  $\approx 30\%$ , for example, being at this level around  $k = 21H_0$ . According to the author [39] this combined four survey approach (SKA1-MID Band 1 and Band 2 IM (intensity mapping) surveys, H $\alpha$  and SKA2) should therefore have sufficient accuracy to distinguish between GR (General Relativity) +  $\Lambda\text{CDM}$  and alternative models, such as coupled quintessence. This accuracy is potentially increased still further through multiple tracer analysis, cross-correlating with other surveys such as Euclid. The combined redshift range for SKA and Euclid is  $0.5 \lesssim z \lesssim 2$ .

Current surveys offer far looser constraints on the growth of structure. Below we use observational data from 6dFGS, LRG<sub>200</sub>, LRG<sub>60</sub>, BOSS, WiggleZ and VIPERS with associated errors [40] in our plots for  $fg$ . These current surveys have a shorter redshift range ( $z \lesssim 0.8$ ) and constrain growth at only  $\approx 10 - 20\%$  level. In single field coupled quintessence there is an observational constraint on the magnitude of the coupling between DE and CDM as  $\mathbb{C} < 0.1\sqrt{\frac{2}{3}}$  [12]. For this class of models couplings greater than this give unrealistic background cosmologies, through deviations in the sound horizon at decoupling from that obtained in  $\Lambda\text{CDM}$  (see e.g. [12]). The McDE models first described in Section V A (1 scalar field and 2 CDM species) give viable background cosmologies through the effect of the opposite charges and symmetric magnitudes of the CDM species [24]. We restrict our background analysis to ensure that the relative background densities match today's values, and that the evolution moves from radiation domination, through a period of CDM domination to a final epoch of DE domination.

#### V. EXAMPLE MODELS

In order to compare models against the standard model, we first applied our code to produce results for the  $\Lambda\text{CDM}$  cosmology. Figure 1 shows the results for the behaviour of  $fg$  together with current observational constraints. We

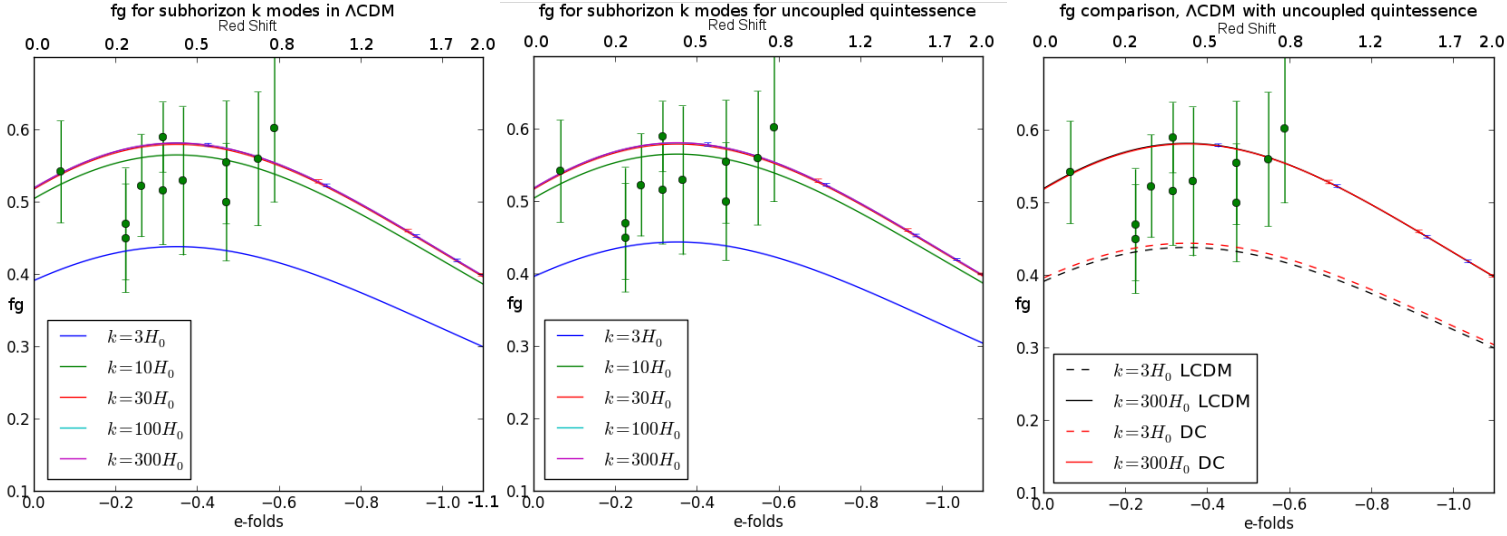


FIG. 1: The left plot shows the growth function,  $fg$ , on sub-horizon scales for  $\Lambda$ CDM, for the region of redshifts relevant for current and future surveys. The green points are observational data from 6dFG S, LRG<sub>200</sub>, LRG<sub>60</sub>, BOSS, WiggleZ and VIPERS with associated errors [40]. The red error bars are the Euclid forecasts and the blue the SKA forecasts [29] applied to the  $k = 300H_0$  plot. The forecast error bars are approximately the line width. The centre plot shows the same for uncoupled two field two CDM species quintessence,  $\lambda = 0.1$ . The right hand plot compares  $fg$  for  $\Lambda$ CDM with uncoupled quintessence (DC) for  $k = 300H_0$  and  $k = 3H_0$ .

also applied our code to a uncoupled quintessence model with two scalar fields and two CDM species. In this case, and for all subsequent models including McDE, the potential for the scalar fields is taken to be a sum of exponentials,

$$V(\varphi_1, \dots, \varphi_I) = M^4 \sum_I e^{-\kappa \lambda_I \varphi_I}, \quad (5.1)$$

where  $\lambda_I$  is the slope of the potential for field  $I$  and  $M$  is the scale of the potential. These results are also shown in Figure 1. We can see that for large  $k$  there is a negligible difference in the growth, and even for small  $k$ , the difference is still too small to be detectable by future surveys such as SKA and Euclid.

### A. Multi-coupled Dark Energy - McDE

Next, we investigated the recently proposed subclass of coupled quintessence, McDE, as described in Refs. [20, 21, 24]. The McDE model has two CDM species coupled to one DE scalar field. The couplings of each DM species have the same magnitude but opposite signs. In order to compare directly with the results of Ref. [24], we set the baryon density to zero for this model. In previous work, perturbations in this model have been studied using an approximation to the full system of equations [12, 16, 22, 24]. This simplification is valid for modes on subhorizon scales and allows scalar field fluctuations to be written in terms of density perturbations. The dimensionality of the system can therefore be reduced and an autonomous system of equations formed for the density perturbations alone. We use the system of ODEs, taken from Ref. [24], to evolve the density perturbations. We also use the same initial conditions to generate results using our implementation of the full equations. This provides a useful examination of the applicability of the subhorizon approximation. Finally, for comparison, we produce  $\Lambda$ CDM results with the assumption of zero baryonic content, using the McDE subhorizon approximations equations and our full system of equations.

We take the initial conditions used in Figure 7 of Ref. [24]. The couplings are symmetric and set to  $\beta = \pm 0.03$  where  $\beta \equiv \left(\sqrt{\frac{3}{2}}\right) \mathbb{C}$  and  $\alpha = 0.12$  where  $\alpha \equiv \lambda$ . The potential is as Eq. (5.1), for  $I = 1$ ,  $\alpha = 2$ . The initial conditions were set non-adiabatically with  $A_{IC} = 2$ , where

$$A_{IC} = \frac{\Omega_- \delta_{-i}}{\Omega_+ \delta_{+i}}, \quad (5.2)$$



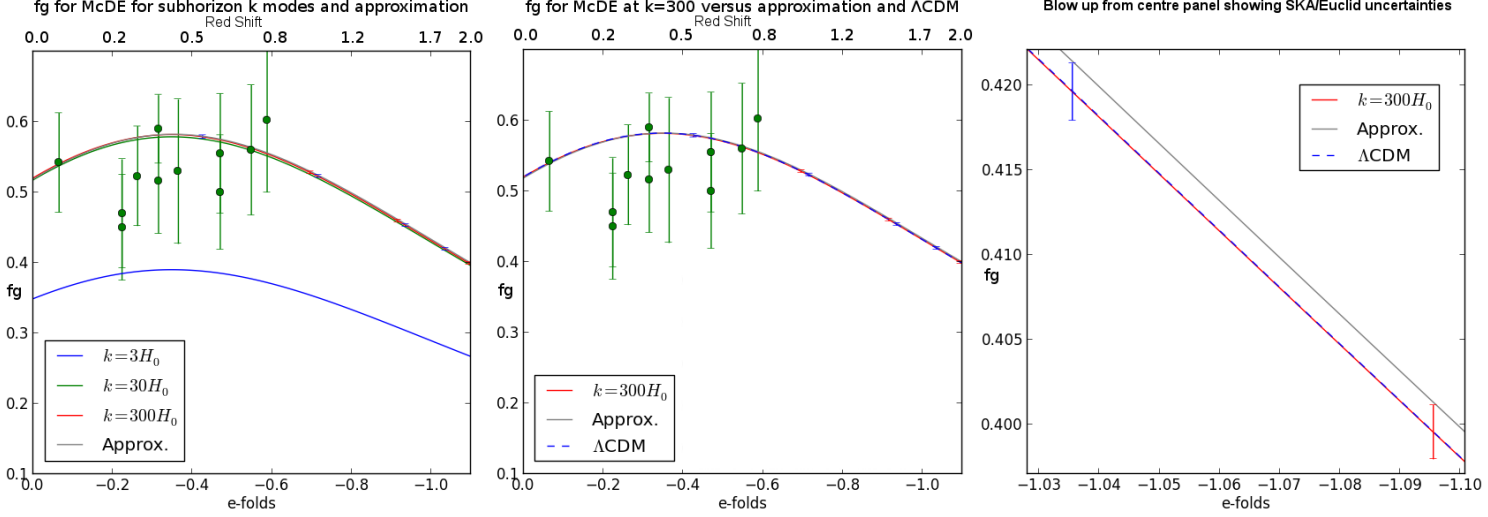


FIG. 2: The left hand panel shows  $fg = \frac{\delta'}{\delta_0}$  for McDE with  $\Omega_\Lambda = 0.692$ , no baryons, one CDM species and unperturbed radiation,  $\lambda = 0.12$ ,  $\mathbb{C} = \pm 0.03\sqrt{\frac{2}{3}}$ . A range of subhorizon  $k$  modes are shown with convergence towards a  $k$  independent evolution of growth with larger  $ks$ . The result for the subhorizon approximation from Ref. [24] is shown in grey. The centre panel shows  $fg$  for McDE for  $k = 300H_0$  for the full equations, the subhorizon approximation from Ref. [24] and  $\Lambda$ CDM for  $k = 300H_0$ . In each panel, the green points are observational data from 6dFGS, LRG<sub>200</sub>, LRG<sub>60</sub>, BOSS, WiggleZ and VIPERS with associated errors [40]. The red error bars are the Euclid forecasts and the blue the SKA forecasts [29] applied to the  $k = 300H_0$  plot. The right panel reproduces a magnified area of the centre panel, showing that the approximation results differ from the full equations by more than the uncertainties.

and  $A_{IC}$  is the measure of the deviation from adiabaticity, ‘-’ denote the negatively charged CDM species and ‘+’ the positively charged. One further parameter is the asymmetry between these two species,  $\mu$ , and is defined

$$\mu = \frac{\Omega_+ - \Omega_-}{\Omega_+ + \Omega_-}. \quad (5.3)$$

Initially  $\mu = 0.5$ , however we found the final results to be insensitive to this initial condition. Once again we generated plots using the reduced system and the full equations for a range of  $ks$ . For quantities which were absent in [24]; radiation perturbations, perturbations to the scalar field, these were initially set to zero.

The results are presented in terms of the evolution of  $fg$  and are shown in Figure 2. For the simplified  $\Lambda$ CDM model, with the baryon content set to zero, and the radiation unperturbed (initially for our full code, while radiation perturbation equations are not included in the subhorizon approximation) the results are shown in Figure 2 together with present and future constraints. Examining this figure, we see that for the largest  $k$  modes the results converge with the result generated using the subhorizon approximation. It should be noted however that there is a noticeable difference in the evolution of growth between the different  $k$  modes down to the scale of  $k = 300H_0$ , and as such the subhorizon approximation is masking this  $k$  dependence over this range of  $ks$ .

As in Ref. [24] we found that the evolution provided by the subhorizon approximation gives an evolution for  $fg$  close to  $\Lambda$ CDM but with a deficit at lower red shifts. The larger  $k$  modes have mostly converged with the approximation, however, there is a small deviation such that at late times  $fg$  is closer to  $\Lambda$ CDM than the approximations. As with all full equation results produced, the growth results are converging with increasing  $k$ , as expected. However, even at scales of  $k = 300H_0$  the small scale approximation appears insufficient for this model, even for the conservative predicted precision for SKA and Euclid measurements. We can see in the right hand plot of Figure 2 that the approximation deviates from the full equations results by more than the predicted observational precision at these higher redshifts. Additionally, for the full equations at  $k = 300H_0$  the evolution of  $fg$  for McDE and  $\Lambda$ CDM models can not be distinguished from the predicted observational precision.

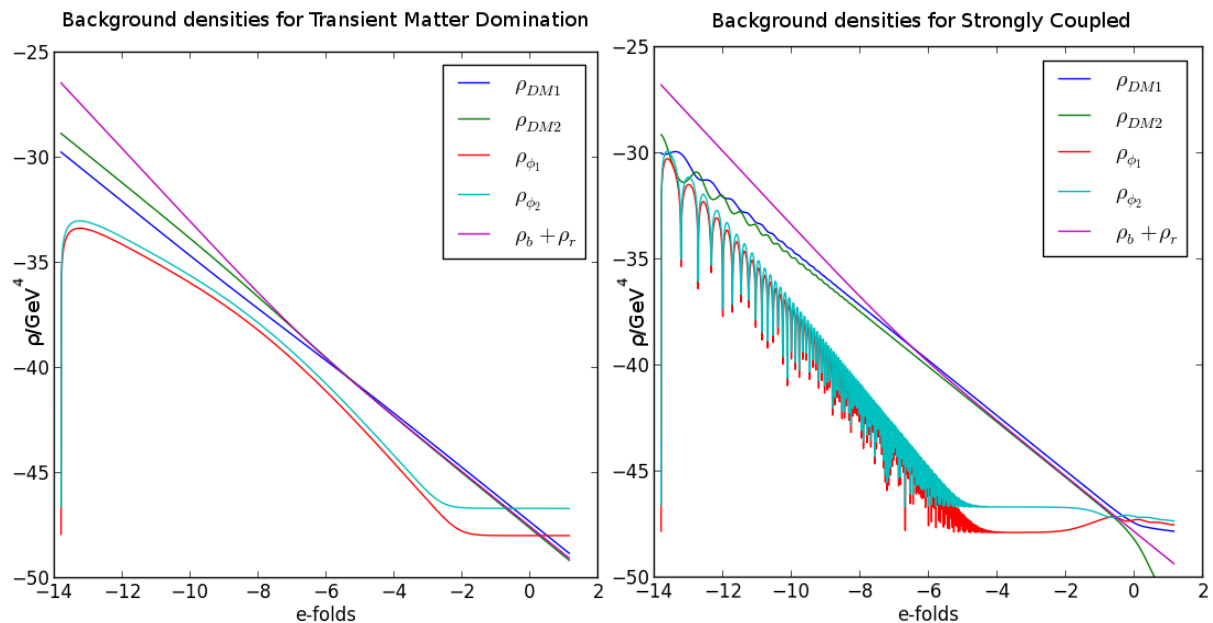


FIG. 3: The left hand plot shows the evolution of the background densities of components for the transient matter domination M $\varphi$ cQ model. The scale is logarithmic. Subscript  $b$  denotes baryons, subscript  $r$  denotes radiation. Couplings,  $\mathbb{C}_{11} = -0.2$ ,  $\mathbb{C}_{12} = 0.4$ ,  $\mathbb{C}_{21} = -0.3$ ,  $\mathbb{C}_{22} = 0.6$ . Slopes for the potentials,  $\lambda_1 = \lambda_2 = 0.1$ . The right hand plot shows the evolution of the background densities of components for the strongly coupled matter dominated coupled quintessence model. Subscript  $b$  denotes baryons, subscript  $r$  denotes radiation. Couplings,  $\mathbb{C}_{11} = -20$ ,  $\mathbb{C}_{12} = 40$ ,  $\mathbb{C}_{21} = -30$  and  $\mathbb{C}_{22} = 60$ . Slopes for the potentials,  $\lambda_1 = \lambda_2 = 10$

## B. Multifield Coupled Quintessence

### 1. Transient Matter Domination

Next we considered the M $\varphi$ cQ model introduced in Ref. [16]. The model contains two pressureless dark matter fluids coupled to two scalar fields. Initially we choose small couplings ( $\mathbb{C}_{11} = -0.2$ ,  $\mathbb{C}_{12} = 0.4$ ,  $\mathbb{C}_{21} = -0.3$  and  $\mathbb{C}_{22} = 0.6$ ) and small slopes for the potentials,  $\lambda_I$  ( $\lambda_1 = \lambda_2 = 0.1$ ). The evolution of the background densities for this model is shown in the left hand panel of Figure 3. These small couplings give rise to a tracking behaviour, by which we mean that the scalar fields densities between  $e$ -folds of within the interval  $-13$  and  $-3$  approximately follow the evolution of the energy densities of the other components. This may alleviate the coincidence problem. This model also still gave a transition to a near constant energy density for the scalar fields at late times and domination of the scalar field energy densities at late times, as required to produce similar background behaviour to  $\Lambda$ CDM.

The right hand panel of Figure 4 is the evolution of  $fg$  for  $k = 300H_0$ , and shows the conservative predicted observational precision would not be enough to distinguish between this model and  $\Lambda$ CDM. However, if optimal performance were achieved leading to an order of magnitude improvement in the observational uncertainties this could be sufficient to distinguish the two models.

### 2. Strongly Coupled Matter Domination

Taking again the same setup, next we choose the couplings  $\mathbb{C}_{11} = -20$ ,  $\mathbb{C}_{12} = 40$ ,  $\mathbb{C}_{21} = -30$  and  $\mathbb{C}_{22} = 60$  and the slopes for the potentials  $\lambda_1 = \lambda_2 = 10$ . The background evolution of this system was also studied in Ref. [16] and can be seen in the right hand plot in Figure 3. The initial oscillations in the scalar fields are caused by the initial conditions for the fields, which are set above the minimum of the effective potential and subsequently oscillate around this minimum. The average behaviour of the scalar fields' energy densities is similar to the transient matter domination model. Initially there is a nearly tracking period at early times, followed by transition to nearly constant energy densities for the fields. Unlike the transient matter domination model, one of the CDM fluids then scales with the scalar fields' energy densities as shown in the right panel of Figure 3. Although there is oscillatory behaviour at

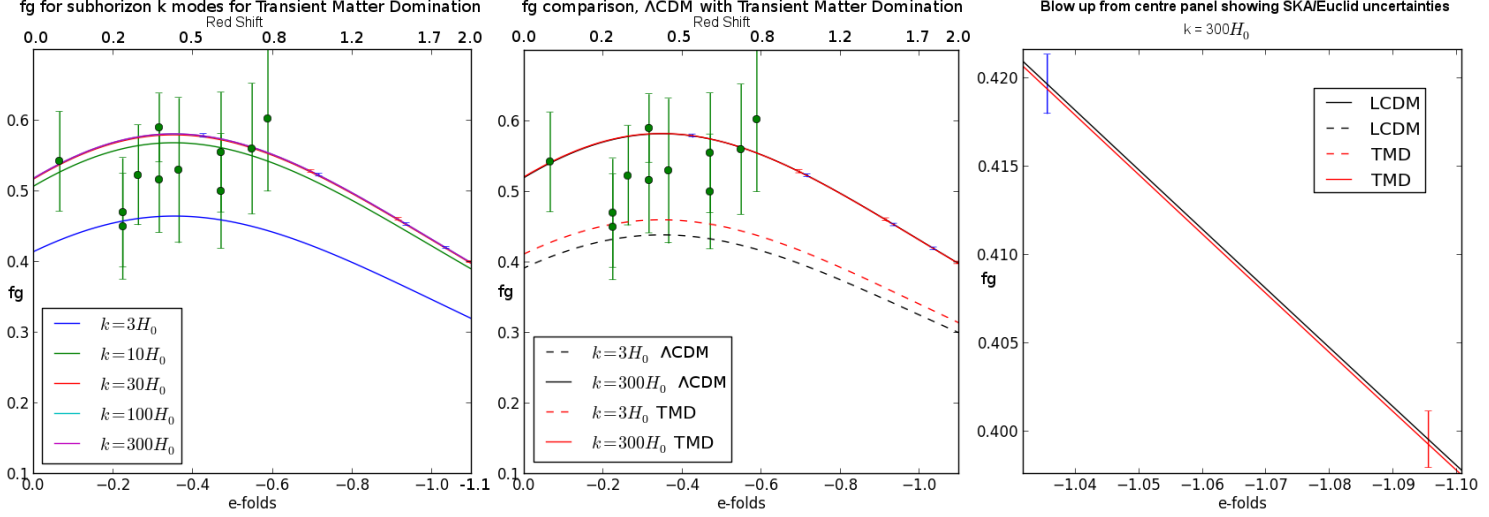


FIG. 4: The left plot shows the growth function,  $fg$ , sub-horizon scales, for the transient matter domination  $M\phi cQ$  model, for the region of redshifts relevant for current and predicted future surveys. Couplings,  $\mathbb{C}_{11} = -0.2$ ,  $\mathbb{C}_{12} = 0.4$ ,  $\mathbb{C}_{21} = -0.3$ ,  $\mathbb{C}_{22} = 0.6$ . Slopes for the potentials,  $\lambda_1 = \lambda_2 = 0.1$ . The green points are observational data from 6dFGS, LRG<sub>200</sub>, LRG<sub>60</sub>, BOSS, WiggleZ and VIPERS with associated errors [40]. The red error bars are the Euclid forecasts and the blue the SKA forecasts [29] applied to the  $k = 300H_0$  plot. The centre plot compares the  $fg$  between  $\Lambda$ CDM and transient matter dominated model (TMD) for  $k = 300H_0$  and  $k = 3H_0$ . The right hand panel zooms in on the centre panel to show the results versus the SKA/Euclid uncertainties for  $k = 300H_0$ .

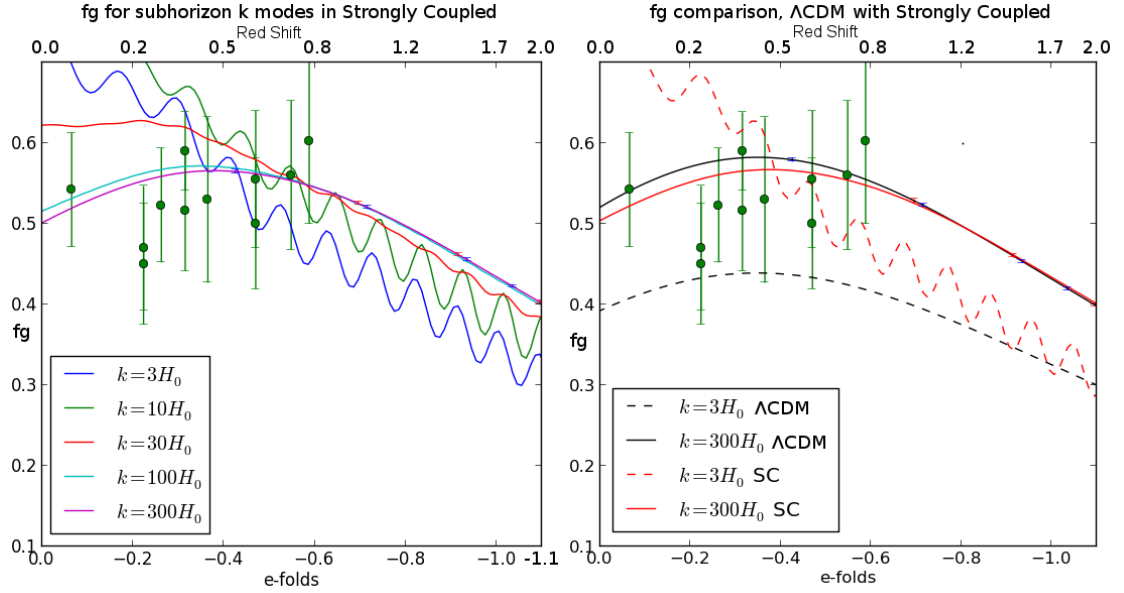


FIG. 5: The left plot shows the growth function,  $fg$ , sub-horizon scales, for strongly coupled matter dominated  $M\phi cQ$  model, for the region of redshifts relevant for current and future surveys. Couplings  $\mathbb{C}_{11} = -0.2$ ,  $\mathbb{C}_{12} = 0.4$ ,  $\mathbb{C}_{21} = -0.3$  and  $\mathbb{C}_{22} = 0.6$ . Slopes for the potentials,  $\lambda_1 = \lambda_2 = 0.1$ . The right hand plot compares the  $fg$  between  $\Lambda$ CDM and the strongly coupled model (SC) for  $k = 300H_0$  and  $k = 3H_0$ .

early times in the growth factor it does not exceed unity, and the average behaviour is very similar to that of the weaker coupled transient matter dominated model. As such the model is consistent with present observations.

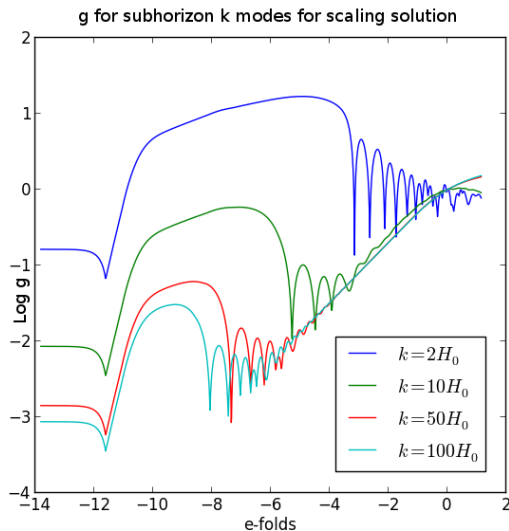


FIG. 6: The plot shows the log of growth factor,  $g$ , for scaling solution  $M\phi cQ$  model, for subhorizon  $k$  modes.

### 3. Scaling Solution

As a second example we followed Ref. [16], and considered the same setup and potential, but chose couplings which give rise to a scaling behaviour. The resultant system is, however, not consistent with observations. It even lacks dark matter domination at earlier epochs. In this example  $\mathbb{C}_{11} = 90$ ,  $\mathbb{C}_{12} = -8$ ,  $\mathbb{C}_{21} = -63$  and  $\mathbb{C}_{22} = -10$  and the slopes of the potentials were taken to be  $\lambda_1 = 10$ ,  $\lambda_2 = 5.4$ . For this example we calculated the growth factor,  $g$ , shown in Figure 6. It can clearly be seen that it becomes greater than unity on subhorizon scales, although less pronounced with increasing  $k$ , showing this model to be unrealistic at both the background and perturbed level.

### 4. Exploration of Potential Slope Space for Strongly Coupled Matter Domination

We now explore how changes in the slopes of the potentials (the  $\lambda_I$  terms in Eq. (5.1)) in the matter dominated model affects the cosmology. Since, for the couplings in the strongly coupled model, the original large value of the slopes,  $\lambda_1 = 10$ ,  $\lambda_2 = 10$  produced excessive growth, we investigated the slope parameter space. This was done from  $\lambda_I = 10$  down to  $\lambda_I = 0.01$ . This region including observationally consistent models is shown in Figure 7.

In producing this figure, the wavenumber of  $k = 42H_0$  was selected since it is the smallest  $k$  mode for which SKA is predicted to still attain its highest precision [39]. The LRG<sub>200</sub> data set was selected simply to serve as an example for comparison (see Section IV for more details on observations used for comparison). Different data sets would move the value of  $f\sigma_8$  slightly, and alter the range of the error bars. There is a range of slopes for which these models not only gave a realistic background cosmology but also gave growth consistent with observations. In this region the parameter values are at least an order of magnitude smaller than the original values used. The background cosmologies for this region are very close in behaviour to Figure 3. For slopes much smaller than  $\lambda = 0.1$  the potential is becoming increasingly flat and the results become noise dominated. As such they were excluded from our analysis.

### 5. Exploration of Couplings Space for Strongly Coupled Matter Domination

For completeness a coarse exploration of the full parameter space of couplings was conducted and the growth function calculated. The range of couplings investigated was from  $-50 \leq \mathbb{C} \leq 50$  with a stepping of 10. The slopes for the potentials and initial conditions were left as before i.e.  $\lambda_1 = \lambda_2 = 10$ . For the portions of coupling space where the couplings satisfied the constraints for these models all exhibited excessive growth.

Finally in Figure 8 we show  $f\sigma_8$  for a sample of the models studied against  $\Lambda$ CDM compared with the SKA and Euclid predicted precisions. This was carried out for mode  $k = 42H_0$  as it corresponds to the largest scale for which

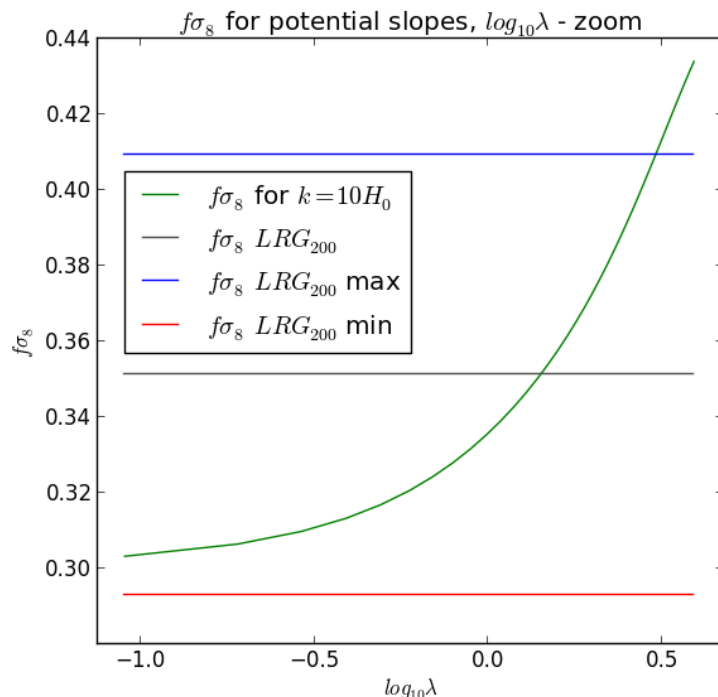


FIG. 7:  $f\sigma_8$  for the matter dominated model with varying slopes for the potentials,  $\lambda$ . The wavenumber was set to  $k = 42H_0$  for these runs. Couplings,  $\mathbb{C}_{11} = -20$ ,  $\mathbb{C}_{12} = 40$ ,  $\mathbb{C}_{21} = -30$ ,  $\mathbb{C}_{22} = 60$ . The observational values with uncertainties used for comparison were those from  $LRG_{200}$ , for  $z = 0.25$ . The plot is a subsection from a region of  $\lambda$  parameter space from  $\lambda = 10$  down to  $\lambda = 0.01$  where the results are consistent with observations.

the highest predicted precision should be achieved for SKA [39]. We can see that unless the best possible predicted precision is achieved it may still be hard to distinguish models with small couplings and slopes from  $\Lambda$ CDM. However, models with larger couplings should be easily identified. The strongly coupled model with  $\lambda_I = 1$  was chosen since it lay within one of the viable regions discovered in Subsection VB 4. For this model it is clear that this would be distinguishable from  $\Lambda$ CDM given even the conservative predicted precision for SKA and Euclid. Therefore, there is a region of parameter space between the transient matter domination parameters and the strongly coupled parameters we initially tested in which subregions satisfy both background constraints and give growth results distinguishable from  $\Lambda$ CDM by future surveys, as the strongly coupled model does.

## VI. CONSISTENCY TEST

The above analysis was performed assuming that the current density parameters are the same as those obtained with Planck data for a  $\Lambda$ CDM cosmology. This approach is simple to implement but may lead to erroneous conclusions because a CMB fit to interacting dark energy models can lead to different density parameters of the various components than the ones obtained assuming  $\Lambda$ CDM (see e.g. Ref. [45]). See also Appendix A of Ref. [46] for a succinct but detailed discussion on this topic.

To ensure the validity of our results, therefore, we undertake a consistency test to confirm that the models studied are sufficiently close to  $\Lambda$ CDM at the time of decoupling and consequently that their background evolutions yield negligible differences. This is of course not entirely sufficient as there is also some contribution from the late integrated Sachs-Wolfe effect brought in by the very recent dark energy domination, nonetheless, the exercise should be informative, given that a full parameter constraint analysis is beyond the scope of this work.

In practice we compared for our different models the value of  $\Omega_M$  at the time of decoupling with the same quantity for  $\Lambda$ CDM, and evaluated whether there is any significant deviation. In the cases where there is a discrepancy we do expect a change in the value of the current energy densities had a CMB fit been carried out. Moreover, a change in the values of the growth factor and of  $fg$  is also to be expected. In this case it is not possible to trust the naive comparison of the results of our study with survey data processed assuming  $\Lambda$ CDM, and a full parameter fit of background and

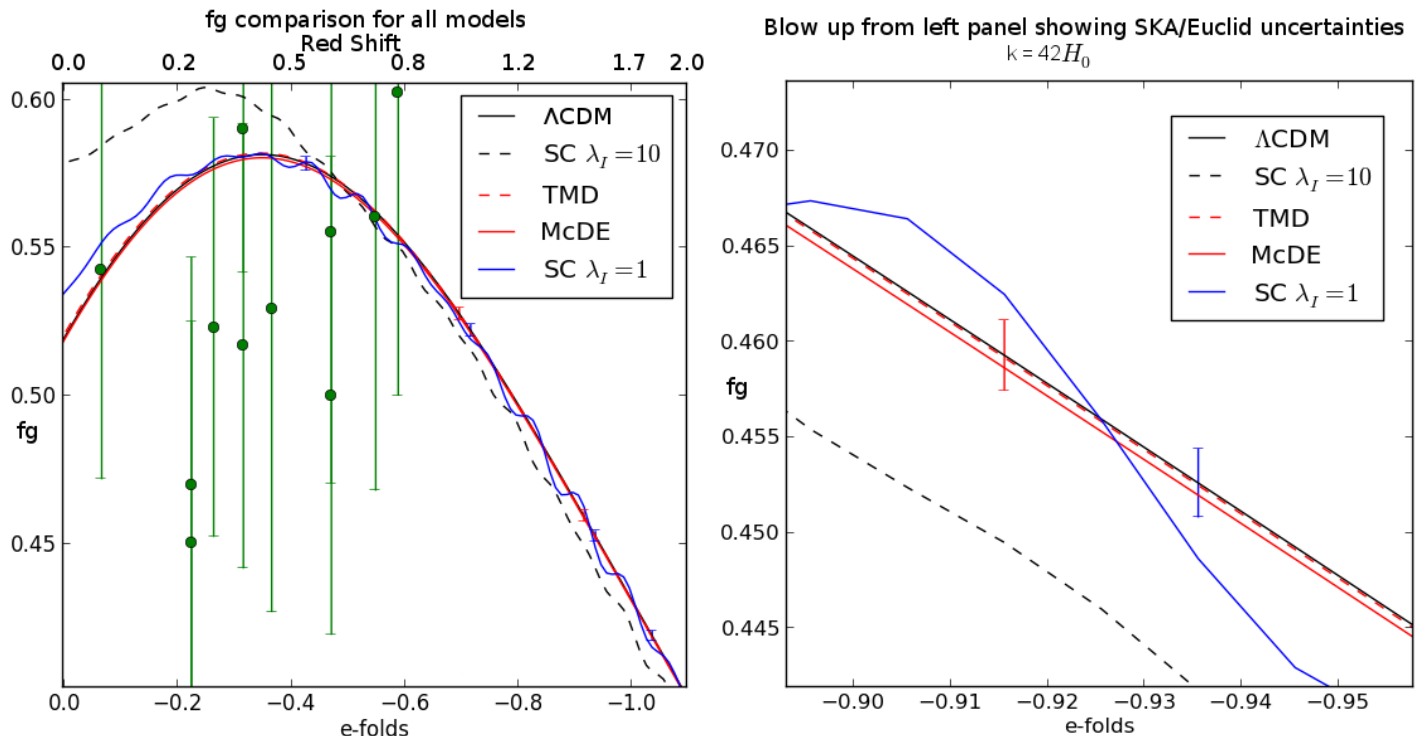


FIG. 8: This plot compares the  $fg$  between  $\Lambda$ CDM and the strongly coupled model (SC) for both  $\lambda_I = 10$  and  $\lambda_I = 1$ , the transient matter dominated model (TMD) and McDE model. All models are evaluated at  $k = 42H_0$ . The insert zooms in on an example region in redshift space where future surveys should measure  $fg$  sufficiently accurately to compare different model predictions.

perturbed parameters would be required.

Given that the McDE model of Section V A has  $\Omega_M$  close to that of  $\Lambda$ CDM at decoupling ( $< 1\%$  deviation), we used this set up as a starting point to investigate the effects of multiple fields on the growth of structure. We show the results in Figure 9. The black dashed line shows an extension to the McDE model, named “McDE 2  $\phi$ ”, where an additional field was added, but with the same magnitude for the couplings and slopes as in the original McDE model in Section V A, i.e.  $C_{11} = 0.024$ ,  $C_{12} = -0.024$ . By comparing with Figure 8, we see that this modification already gives a larger difference in the growth from  $\Lambda$ CDM than for the original McDE model. However, although the value of  $\Omega_M$  at decoupling deviates from the one of the  $\Lambda$ CDM model by less than 1%, it is not as close to  $\Lambda$ CDM as the original McDE model, and for the purposes of the validity of our analysis we seek models which match  $\Lambda$ CDM  $\Omega_M$  at decoupling exactly. This was achieved by adjusting the couplings of the McDE 2  $\phi$  model such that  $C_{11} = C_{21} = 0.095$ ,  $C_{12} = C_{22} = -0.095$  and  $\lambda_I = 0.1$ . This model, named “McDE 2  $\phi$ -A”, corresponds to the red dashed line in Figure 9. While this has the same value for  $\Omega_M$  at decoupling to  $\Lambda$ CDM, the growth deviated from this by more than the SKA and Euclid uncertainties at the redshifts shown.

As a third example we have considered a modified TMD model. By this we mean that for each CDM species coupling to a given field the couplings are of equal magnitude and opposite sign, but differ in magnitude between the fields. We named this model “TMD-A”, represented with a blue solid line in Figure 9. More specifically, the couplings are  $C_{11} = 0.07$ ,  $C_{12} = -0.07$ ,  $C_{21} = 0.12$  and  $C_{22} = -0.12$  and  $\lambda_I = 0.1$ . This also gives identical  $\Omega_M$  at decoupling to  $\Lambda$ CDM, while the growth deviates from the growth in  $\Lambda$ CDM by more than the SKA and Euclid uncertainties at the redshifts shown, and slightly more than all the other models shown. The SKA and Euclid uncertainties are themselves at the 1% level and we are therefore confident that the growth for these models should be distinguishable from that predicted by  $\Lambda$ CDM by these future surveys.

## VII. DISCUSSION AND CONCLUSION

In this paper we have presented the full equations for perturbations in  $M\phi cQ$  models, produced a numerical package to evolve these perturbations, PYESSENCE, and used this package to compare a set of example models with

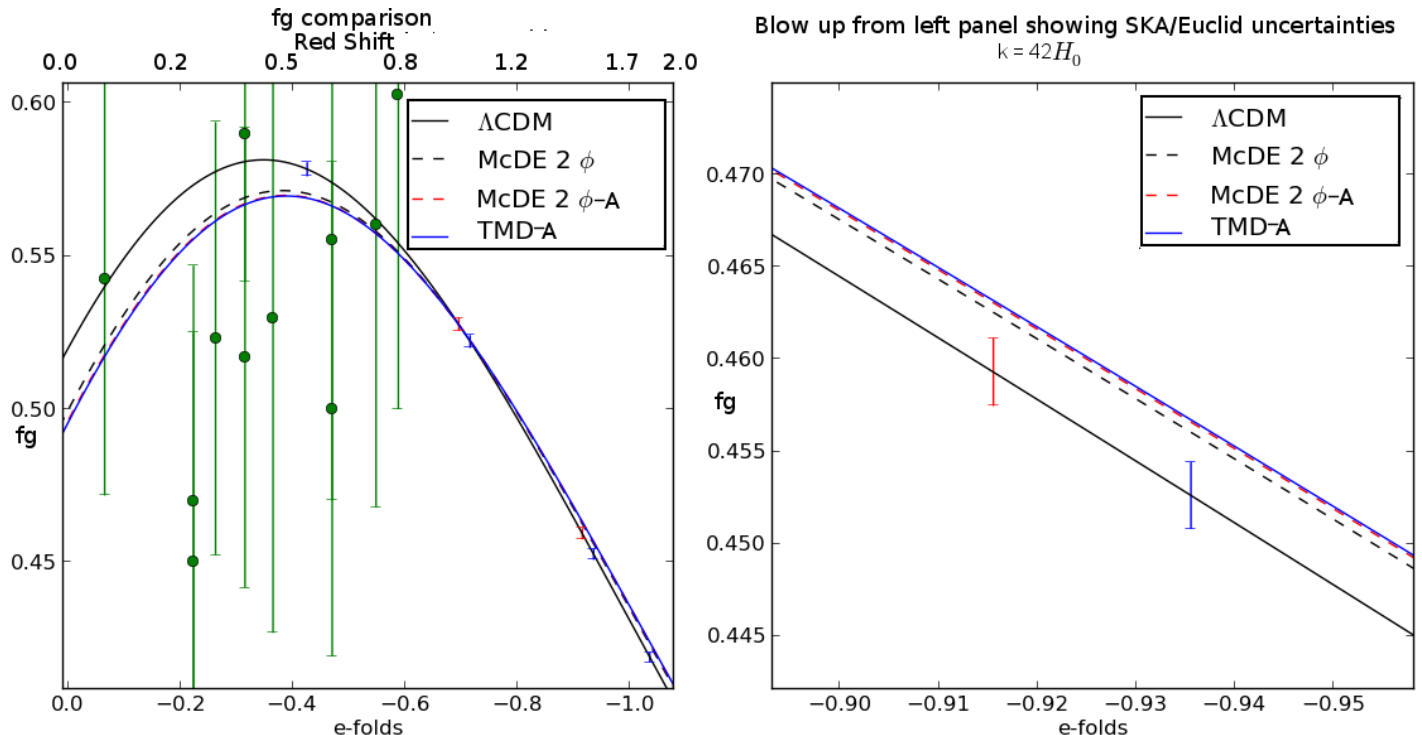


FIG. 9: These plots compare the  $fg$  between  $\Lambda$ CDM and various iterations of the TMD and McDE models. All models are evaluated at  $k = 42H_0$ . The right hand plot zooms in on an example region in redshift space where future surveys should measure  $fg$  sufficiently accurately to compare different model predictions. The black solid line is for McDE as defined in Section V A but with an additional field with the same size slopes and couplings to the matter species. The red dashed line is the same model with larger couplings of  $\pm 0.095$  and slopes of  $\lambda_I = 0.1$ . Finally the blue solid line is a “balanced” TMD model with couplings of  $+0.07, -0.07, +0.12$  and  $-0.12$  and  $\lambda_I = 0.1$ .

observations. We found that the longitudinal gauge, often employed in previous studies of less general systems, is not ideal for the numerical evolution of the full system, and we therefore used the flat gauge.

We found that there are examples of  $M\phi cQ$  models which lie within current observational bounds, however, distinguishable from  $\Lambda$ CDM models with future surveys such as Euclid and SKA, as they will attain a precision in  $fg$  at the percent level or better [29]. On the other hand, we also found examples such as the strongly coupled model defined in Ref. [16], where  $fg$  is incompatible with current observations, ruling out the model. This confirms the conclusion in Ref. [16], that while “large” couplings might give a realistic background model, the perturbations experience excessively strong growth (or damping) and are, therefore, unrealistic. However, we found that it did not require both the couplings and the slopes to be reduced simultaneously in order for a region of viable background and perturbed cosmologies to be recovered, as discussed in Subsection V B 4, since when  $\lambda \lesssim 2$  this leads to a viable parameter space region.

We have found for the McDE model, and the transient matter dominated case for the  $M\phi cQ$  models studied, that they give realistic background cosmologies while apparently exceeding the allowed coupling strength for single field  $M\phi cQ$ ,  $C \lesssim 0.1\sqrt{\frac{2}{3}}$  (see e.g. Ref. [12]). This difference in behaviour between single field (and single CDM species) and multiple CDM species models results from the relative signs of the couplings. In Ref. [24], the McDE model with couplings significantly greater than  $0.1\sqrt{\frac{2}{3}}$  gave rise to viable background and perturbed cosmologies. This is attributed to the unique way in which the CDM species are oppositely charged with respect to the DE scalar field (couplings are also of the same magnitude). In our  $M\phi cQ$  models each CDM species has an opposite charge relative to each scalar field i.e. CDM species 1 has a negative coupling to scalar field 1 while CDM species 2 has a positive coupling, and similarly for scalar field 2. Although the couplings are no longer symmetric in magnitude, this partial balance of charge still has a similar effect as in McDE, both in giving viable background cosmologies and in controlling the growth of structure. However, of the models studied only the transient matter dominated model satisfied both the background evolution and the evolution of growth through  $fg$  for low redshift.

Finally, we have also addressed the question of the applicability of the large  $k$  approximation, and investigated at



which scales it may be considered a good approximation. The deviation of the full equation results for large  $k$  modes from the approximation is frequently greater than the experimental uncertainty in future surveys. In Section V A we showed that using a subhorizon approximation gave a difference in results for growth from the full equations which would be larger than the predicted observational precision for SKA and Euclid. The approximation already deviates from the full equations by more than the predicted precision of SKA [39] at  $k = 300H_0$  and becomes progressively worse towards  $k = 42H_0$ , the boundary for which SKA is predicted to have the highest precision. Hence results from the full equations should be used for comparison with future observations instead of those obtained using the approximation. This is therefore an important aspect to take into account in the analysis of large scale structure from near future experiments.

### Acknowledgments

The authors are grateful to Ian Huston, Pedro Carrilho, Phil Bull and Shailee Imrith for helpful discussions. AL is funded by a STFC studentship, KAM is supported, in part, by STFC grant ST/M001202/1 and DJM is supported by a Royal Society University Research Fellowship. N.J.N thanks Queen Mary University of London for hospitality. His research work is supported by the grant UID/FIS/04434/2013. The computer algebra package CADABRA[42] was used in the derivation of some of the equations.

## Appendix A: Gauge Transformations

### 1. General Gauge Transformations

We now give the gauge transformations for the perturbed quantities used in the main body of this paper and in Subsection A 2 below. Following the notation of Ref. [32], quantities in the new coordinate system are denoted by a tilde.

The matter variables, the velocity and the density perturbations, transform as

$$\tilde{v}_\alpha = \hat{v}_\alpha + \frac{\delta t}{a}, \quad (\text{A1})$$

$$\tilde{\delta\rho}_\alpha = \delta\rho_\alpha - \dot{\rho}_\alpha \delta t, \quad (\text{A2})$$

where  $\hat{v}_\alpha$  is defined in Eq. (2.24).

The perturbations of the metric transform as

$$\tilde{\phi} = \phi - \dot{\delta}t, \quad (\text{A3})$$

$$\tilde{\psi} = \psi + H\delta t, \quad (\text{A4})$$

$$\tilde{B} = B - a\dot{\delta}x + \delta t, \quad (\text{A5})$$

$$\tilde{E} = E - \delta x. \quad (\text{A6})$$

### 2. Flat to Longitudinal Gauge Relations

The relation between the velocity in flat and in longitudinal gauge is given by

$$\hat{v}_{\alpha(\text{flat})} = v_{\alpha(\text{long})} + B_{(\text{flat})}. \quad (\text{A7})$$

The relation for the density perturbations is

$$\delta\rho_{\alpha(\text{flat})} = \delta\rho_{\alpha(\text{long})} - a\dot{\rho}_\alpha B_{(\text{flat})}. \quad (\text{A8})$$

The transformation behaviour of the metric perturbations and the fact that  $\phi = \psi$  in longitudinal gauge in the absence of anisotropic stress gives

$$B_{(\text{flat})} = -\frac{\phi_{(\text{long})}}{Ha}. \quad (\text{A9})$$



## Appendix B: Longitudinal Gauge with with Arbitrary Numbers of Fields and DM Fluids

As mentioned in Section II B 2 the PYESENCE code was originally written in longitudinal gauge as this is one commonly used in literature in the field, see e.g. [16]. However due to numerical instabilities caused by the constraint Eq. (B8) for  $\phi$  below, this version was abandoned. We include the equations below for reference and completeness.

For a given DM species,  $\alpha$ , the evolution equation for the perturbation is

$$\delta\dot{\rho}_\alpha + 3H(\delta\rho_\alpha + \delta P_\alpha) - \left(3\dot{\phi} + \frac{k^2 v_\alpha}{a}\right)(\bar{\rho}_\alpha + \bar{P}_\alpha) = -\sum_I \kappa \mathbb{C}_{I\alpha}(\bar{\rho}_\alpha - 3\bar{P}_\alpha)\delta\dot{\varphi}_I - \sum_I \kappa \mathbb{C}_{I\alpha}(\delta\rho_\alpha - 3\delta P_\alpha)\dot{\bar{\varphi}}_I. \quad (\text{B1})$$

Momentum conservation is given by

$$\dot{v}_\alpha = \kappa \sum_I \mathbb{C}_{I\alpha}(\bar{\rho}_\alpha - 3\bar{P}_\alpha)\frac{\delta\varphi_I}{a} + 3H\frac{\dot{\bar{P}}_\alpha}{\dot{\bar{\rho}}_\alpha}(v_\alpha) - H(v_\alpha) - \frac{\phi}{a} - \frac{\delta P_\alpha}{a(\bar{\rho}_\alpha + \bar{P}_\alpha)}. \quad (\text{B2})$$

The evolution equation for the fields, labelled  $I, J$ , is

$$\delta\ddot{\varphi}_I + 3H\delta\dot{\varphi}_I + \sum_J V_{,\varphi_I\varphi_J}\delta\varphi_J - 4\dot{\phi}\dot{\bar{\varphi}}_I + \frac{k^2}{a^2}\delta\varphi_I + 2V_{,\varphi_I}\phi - 2\sum_\alpha \kappa \mathbb{C}_{I\alpha}(\bar{\rho}_\alpha - 3\bar{P}_\alpha)\phi - \sum_\alpha \kappa \mathbb{C}_{I\alpha}(\delta\rho_\alpha - 3\delta P_\alpha) = 0. \quad (\text{B3})$$

The Einstein Field Equations are as follows. From the  $0-0$  component we get

$$3H(\dot{\phi} + H\phi) + \frac{k^2}{a^2}\phi = -\frac{\kappa^2}{2}\left[\sum_\alpha \delta\rho_\alpha + \sum_I (-\phi\dot{\bar{\varphi}}_I^2 + \delta\dot{\varphi}_I\dot{\bar{\varphi}}_I + V_{,\varphi_I}\delta\varphi_I)\right]. \quad (\text{B4})$$

From the  $0-i$  component we get

$$\dot{\phi} + H\phi = -\frac{\kappa^2}{2}\left[\sum_\alpha av_\alpha(\bar{\rho}_\alpha + \bar{P}_\alpha) - \sum_I \dot{\bar{\varphi}}_I\delta\varphi_I\right]. \quad (\text{B5})$$

From the trace of  $i-j$  component we get

$$\ddot{\phi} + 4H\dot{\phi} + (3H^2 + 2\dot{H})\phi = \frac{\kappa^2}{2}\left[\sum_\alpha \delta P_\alpha - \sum_I (\phi\dot{\bar{\varphi}}_I^2 - \delta\dot{\varphi}_I\dot{\bar{\varphi}}_I + V_{,\varphi_I}\delta\varphi_I)\right]. \quad (\text{B6})$$

From the trace-free part of the  $i-j$  component we get

$$\psi = \phi, \quad (\text{B7})$$

since  $\sigma_s = 0$ .

From Eq. (B4) and Eq. (B5) we get

$$\phi = \left(\sum_I \dot{\bar{\varphi}}_I^2 - \frac{2k^2}{(\kappa a)^2}\right)^{-1}\left[\sum_\alpha (\delta\rho_\alpha - 3Hav_\alpha(\bar{\rho}_\alpha + \bar{P}_\alpha)) + \sum_I (\delta\dot{\varphi}_I\dot{\bar{\varphi}}_I + V_{,\varphi_I}\delta\varphi_I + 3H\dot{\bar{\varphi}}_I\delta\varphi_I)\right] \quad (\text{B8})$$

## Appendix C: Synchronous Comoving Gauge with Arbitrary Numbers of Fields and DM Fluids

Synchronous gauge had been considered for use in the PYESENCE code. This was partly because it has been used in codes such as CAMB and CLASS [43, 44]. The equations from Section II B are presented here in synchronous co-moving gauge ( $\tilde{\phi} = \tilde{B} = \tilde{v} = 0$ ), but otherwise in full generality, allowing for multiple fields and fluids. This is done for reference and completeness. For a given DM species,  $\alpha$ , the evolution equation for the perturbation is

$$\delta\dot{\rho}_\alpha + 3H(\delta\rho_\alpha + \delta P_\alpha) - (3\dot{\psi} + k^2\dot{E})(\bar{\rho}_\alpha + \bar{P}_\alpha) = -\sum_I \kappa \mathbb{C}_{I\alpha}(\bar{\rho}_\alpha - 3\bar{P}_\alpha)\delta\dot{\varphi}_I - \sum_I \kappa \mathbb{C}_{I\alpha}(\delta\rho_\alpha - 3\delta P_\alpha)\dot{\bar{\varphi}}_I. \quad (\text{C1})$$

Momentum conservation is given by

$$\kappa \sum_I \mathbb{C}_{I\alpha} (\bar{\rho}_\alpha - 3\bar{P}_\alpha) \delta\varphi_I = \frac{\delta P_\alpha}{\bar{\rho}_\alpha + \bar{P}_\alpha}. \quad (\text{C2})$$

The evolution equation for the fields, labelled  $I, J$ , is

$$\ddot{\delta\varphi}_I + 3H\dot{\delta\varphi}_I + \sum_J V_{,\varphi_I\varphi_J} \delta\varphi_J - (3\dot{\psi} + k^2\dot{E}) \dot{\varphi}_I + \frac{k^2}{a^2} \delta\varphi_I - \sum_\alpha \kappa \mathbb{C}_{I\alpha} (\delta\rho_\alpha - 3\delta P_\alpha) - 2\kappa \sum_\alpha \mathbb{C}_{I\alpha} \bar{\rho}_\alpha = 0. \quad (\text{C3})$$

The Einstein Field Equations are as follows. From the  $0-0$  component we get

$$3H(\dot{\psi}) + \frac{k^2}{a^2} (\psi + Ha^2\dot{E}) = -\frac{\kappa^2}{2} \left[ \sum_\alpha \delta\rho_\alpha + \sum_I (\dot{\delta\varphi}_I \dot{\varphi}_I + V_{,\varphi_I} \delta\varphi_I) \right]. \quad (\text{C4})$$

From the  $0-i$  component we get

$$\dot{\psi} = \frac{\kappa^2}{2} \sum_I \dot{\varphi}_I \delta\varphi_I. \quad (\text{C5})$$

From the trace of  $i-j$  component we get

$$\ddot{\psi} + 3H\dot{\psi} = \frac{\kappa^2}{2} \left[ \sum_\alpha \delta P_\alpha + \sum_I (\dot{\delta\varphi}_I \dot{\varphi}_I - V_{,\varphi_I} \delta\varphi_I) \right]. \quad (\text{C6})$$

From the trace-free part of the  $i-j$  component we get

$$\dot{\sigma}_s + H\sigma_s + \psi = 0, \quad (\text{C7})$$

where  $\sigma_s$  is the scalar shear and  $\sigma_s = a^2\dot{E}$ .

- 
- [1] R. Adam *et al.* [Planck Collaboration], arXiv:1502.01582 [astro-ph.CO].
  - [2] J. Dunkley, R. Hlozek, J. Sievers, V. Acquaviva, P. A. R. Ade, P. Aguirre, M. Amiri and J. W. Appel *et al.*, *Astrophys. J.* **739**, 52 (2011) [arXiv:1009.0866 [astro-ph.CO]].
  - [3] N. R. Hall, L. Knox, C. L. Reichardt, P. A. R. Ade, K. A. Aird, B. A. Benson, L. E. Bleem and J. E. Carlstrom *et al.*, *Astrophys. J.* **718**, 632 (2010) [arXiv:0912.4315 [astro-ph.CO]].
  - [4] S. Perlmutter *et al.* [Supernova Cosmology Project Collaboration], *Astrophys. J.* **517**, 565 (1999) [astro-ph/9812133].
  - [5] A. G. Riess *et al.* [Supernova Search Team Collaboration], *Astron. J.* **116**, 1009 (1998) [astro-ph/9805201].
  - [6] M. Kowalski *et al.* [Supernova Cosmology Project Collaboration], *Astrophys. J.* **686**, 749 (2008) doi:10.1086/589937 [arXiv:0804.4142 [astro-ph]].
  - [7] L. Anderson *et al.* [BOSS Collaboration], arXiv:1312.4877 [astro-ph.CO].
  - [8] C. Bonnett *et al.* [DES Collaboration], arXiv:1507.05909 [astro-ph.CO].
  - [9] K. S. Dawson *et al.*, arXiv:1508.04473 [astro-ph.CO].
  - [10] L. Amendola, *Mon. Not. Roy. Astron. Soc.* **312**, 521 (2000) [astro-ph/9906073].
  - [11] D. J. Holden and D. Wands, *Phys. Rev. D* **61**, 043506 (2000) [gr-qc/9908026].
  - [12] L. Amendola, *Phys. Rev. D* **62**, 043511 (2000) [astro-ph/9908023].
  - [13] T. Koivisto, *Phys. Rev. D* **72**, 043516 (2005) [astro-ph/0504571].
  - [14] T. Gonzalez, G. Leon and I. Quiros, *Class. Quant. Grav.* **23**, 3165 (2006) [astro-ph/0702227].
  - [15] J. Valiviita, E. Majerotto and R. Maartens, *JCAP* **0807**, 020 (2008) [arXiv:0804.0232 [astro-ph]].
  - [16] L. Amendola, T. Barreiro and N. J. Nunes, arXiv:1407.2156 [astro-ph.CO].
  - [17] G. R. Farrar and P. J. E. Peebles, *Astrophys. J.* **604**, 1 (2004) [astro-ph/0307316].
  - [18] E. J. Copeland, N. J. Nunes and M. Pospelov, *Phys. Rev. D* **69**, 023501 (2004) [hep-ph/0307299].
  - [19] A. W. Brookfield, C. van de Bruck and L. M. H. Hall, *Phys. Rev. D* **77**, 043006 (2008) [arXiv:0709.2297 [astro-ph]].
  - [20] M. Baldi, *Annalen Phys.* **524**, 602 (2012) [arXiv:1204.0514 [astro-ph.CO]].
  - [21] A. Piloyan, V. Marra, M. Baldi and L. Amendola, *JCAP* **1307**, 042 (2013) [arXiv:1305.3106 [astro-ph.CO]].
  - [22] L. Amendola, S. Tsujikawa Cambridge, UK: Univ. Pr. (2010) 503 p
  - [23] T. S. Koivisto, E. N. Saridakis and N. Tamanini, *JCAP* **1509**, 047 (2015) doi:10.1088/1475-7516/2015/09/047 [arXiv:1505.07556 [astro-ph.CO]].

- [24] A. Piloyan, V. Marra, M. Baldi and L. Amendola, JCAP **1402**, 045 (2014) [arXiv:1401.2656 [astro-ph.CO]].
- [25] A. R. Liddle, A. Mazumdar and F. E. Schunck, Phys. Rev. D **58**, 061301 (1998) [astro-ph/9804177].
- [26] K. A. Malik and D. Wands, Phys. Rev. D **59**, 123501 (1999) doi:10.1103/PhysRevD.59.123501 [astro-ph/9812204].
- [27] P. Kanti and K. A. Olive, Phys. Rev. D **60**, 043502 (1999) doi:10.1103/PhysRevD.60.043502 [hep-ph/9903524].
- [28] T. D. Kitching *et al.*, arXiv:1501.03978 [astro-ph.CO].
- [29] A. Raccanelli *et al.*, arXiv:1501.03821 [astro-ph.CO].
- [30] G. D'Amico, T. Hamill and N. Kaloper, arXiv:1605.00996 [hep-th].
- [31] M. C. D. Marsh, arXiv:1606.01538 [astro-ph.CO].
- [32] K. A. Malik and D. Wands, JCAP **0502**, 007 (2005) [astro-ph/0411703].
- [33] <https://bitbucket.org/pyessence/pyessence>
- [34] <http://pyessence.leithes.co.uk/>
- [35] A. Leithes, arXiv:1608.00910
- [36] P. A. R. Ade *et al.* [Planck Collaboration], arXiv:1502.01589 [astro-ph.CO].
- [37] A. R. Liddle and D. H. Lyth, Cambridge, UK: Univ. Pr. (2000) 400 p
- [38] P. A. R. Ade *et al.* [Planck Collaboration], Astron. Astrophys. **594**, A20 (2016) doi:10.1051/0004-6361/201525898 [arXiv:1502.02114 [astro-ph.CO]].
- [39] P. Bull, Astrophys. J. **817**, no. 1, 26 (2016) doi:10.3847/0004-637X/817/1/26 [arXiv:1509.07562 [astro-ph.CO]].
- [40] E. Macaulay, I. K. Wehus and H. K. Eriksen, Phys. Rev. Lett. **111**, no. 16, 161301 (2013) [arXiv:1303.6583 [astro-ph.CO]].
- [41] T. Abbott *et al.* [DES Collaboration], arXiv:1507.05552 [astro-ph.CO].
- [42] K. Peeters, Comput. Phys. Commun. **176**, 550 (2007) [arXiv:cs/0608005]. K. Peeters, arXiv:hep-th/0701238.
- [43] A. Lewis, A. Challinor and A. Lasenby, Astrophys. J. **538**, 473 (2000) [astro-ph/9911177].
- [44] D. Blas, J. Lesgourgues and T. Tram, JCAP **1107**, 034 (2011) [arXiv:1104.2933 [astro-ph.CO]].
- [45] J. Väliiviita and E. Palmgren, JCAP **1507**, no. 07, 015 (2015) doi:10.1088/1475-7516/2015/07/015 [arXiv:1504.02464 [astro-ph.CO]].
- [46] E. Jennings, C. M. Baugh, R. E. Angulo and S. Pascoli, Mon. Not. Roy. Astron. Soc. **401**, 2181 (2010) doi:10.1111/j.1365-2966.2009.15819.x [arXiv:0908.1394 [astro-ph.CO]].